Understanding Inchworm Crawling for Soft-Robotics

Benny Gamus, Lior Salem, Amir D. Gat, and Yizhar Or

arXiv:1911.05227v2 [cond-mat.soft] 17 Nov 2019

Abstract—**Crawling is a common locomotion mechanism in soft robots and nonskeletal animals. In this work we propose modeling soft-robotic legged locomotion by approximating it with an equivalent articulated robot with elastic joints. For concreteness we study the inchworm crawling of our soft robot with two bending actuators, via an articulated three-link model. The solution of statically indeterminate systems with stick-slip contact transitions requires for a novel hybrid-quasistatic analysis. Then, we utilize our analysis to investigate the influence of phase-shifted harmonic inputs on performance of crawling gaits, including sensitivity analysis to friction uncertainties and energetic cost of transport. We achieve optimal values of gait parameters. Finally, we fabricate and test a fluid-driven soft robot. The experiments display good agreement with the theoretical analysis, proving that our simple model correctly captures and explains the fundamental principles of inchworm crawling and can be applied to other soft-robotic legged robots.**

I. INTRODUCTION

In nature, many soft-bodied creatures are capable of complex locomotion in challenging environments, inaccessible to skeletal animals [1]. Their ability to squeeze through gaps smaller than their unconstrained body dimensions has been one of the motivations for the emerging bio-inspired field of *soft robotics* [2], [3].

Inchworm crawling is a common locomotion mechanism among soft animals [1], [4] and robots [5]–[11], characterized by alternating stick-slip transitions of the contact points while maintaining ground contact. The actual inchworm and similar biological creatures use sophisticated methods, like gripping spines, to actively change the contact interaction [12]. This is implemented in some robots by active adhesion [13] or active directional friction manipulation [5], [8], [11], [14] while others perform crawling locomotion with passive frictional contacts [7], [9]. It is also typical that crawling soft robots and animals move rather slowly (relatively to their dynamic natural frequencies), such that the inertial effects are negligible, and they transition within a continuum of *static* equilibria. Hence, the focus of this work is quasistatic locomotion. The mentioned examples may also be classified as bipedal robots, since they crawl on two contacts.

Creating soft-robotic locomotion in a desired pattern involves increased complexity and requires theoretical modeling. In soft-robotic actuators and manipulators, most works suggest kinematic models for control, obtained either empirically [15]–[17] or from static elasticity theories [18]–[20] and few studies

suggest dynamic models [21]–[23]. In soft-robotic crawling and walking, some works rely on kinematic modeling of a soft actuator for control [24], [25] while the field is mostly dominated by an experimental approach [6], [26], which is very limited. For example, the high sensitivity of soft-robotic gaits to variations in friction was shown in [27]. In legged robotics, theoretical models and analysis of the locomotion are
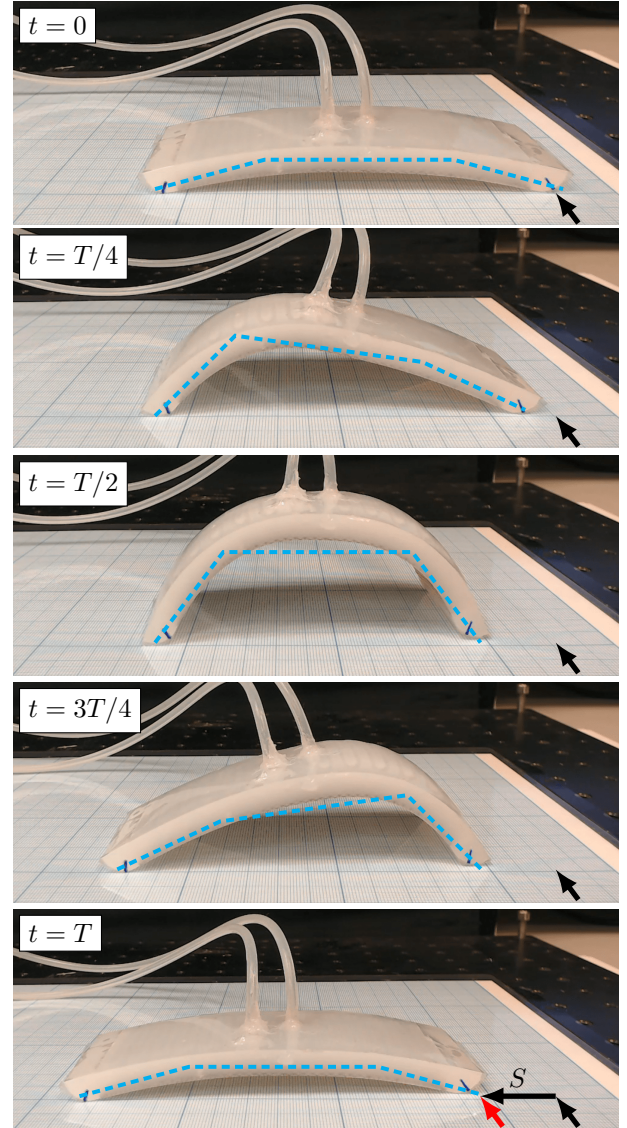

Fig. 1: Time-snapshots of a single inchworm-like period of our fluid-driven soft robot with two phase-shifted periodic inputs (T is period time, dashed cyan lines denote the equivalent three-link model)

Benny Gamus, Amir D. Gat and Yizhar Or are with the Faculty of Mechanical Engineering, Technion – Israel Institute of Technology, Technion City, Haifa, Israel 3200003.

Lior Salem, Amir D. Gat and Yizhar Or are also with the Technion Autonomous Systems Program, Technion - Israel Institute of Technology, Technion City, Haifa, Israel 3200003.

essential for design of the gait and the robot's structure and in the pursuit of robots capable of dynamic movements. This was demonstrated by few lumped models [28]–[30], which showed applications to numerical control and gait optimization. Some other studies also suggested theoretical modeling ideas [31], [32] and discretization method for a large-dimensional computational model [33].

For intuitive comprehension and analysis of the soft-robotic legged locomotion, particularly inchworm crawling, we aim to achieve a low-dimensional lumped model. A common modeling approach in the field of mechanisms with compliant elements is approximating the stiffness of the elastic parts by lumped springs interconnecting rigid links [34]. This was utilized in some articulated robots [35], [36] and in a limited way in soft robotics [37]. Our work presents the application of this modeling approach, including the stick-slip contact transitions [31]–[33], on soft-robotic quasistatic legged locomotion. Specifically, we analyze a three-link robot as a model of inchworm crawling of a soft bipedal robot (see Fig. 1) – which, according to our experiments, captures well the major phenomena. To the best of our knowledge, the frictional crawling of a three-link robot has not been previously studied, though being a very basic form of multi-contact bipedal locomotion, in analogy to McGeer's biped [38] being a basic form a of bipedal walking. The only exception is perhaps [39], which have exploited a similar mechanism to study the properties of dogs' walking gaits.

Problem introduction

We now present our soft-robotic bipedal prototype, for concrete illustration of the proposed modeling approach and experimental validation. The soft robot in Fig. 1 consists of two separately controlled continuous soft-robotic actuators, each causing bending of the respective segment. We implement the bending actuators by embedded slender fluidic networks [23], [40] as illustrated in Fig. 2 and described in Section III. Nevertheless, the ideas and analysis presented in this paper are applicable to any bending actuators. When introducing periodic pressure inputs with a phase shift into the two channel segments, a progression pattern emerges as depicted by the time-snapshots in Fig. 1. Similar results were observed in other inchworm-like robots [6], but the design of the inputs in literature is mostly done by trial and error. The purpose of this study is to model and understand the mechanism behind frictional crawling for improved gait-planning and structural design.

The main contributions of our work are as follows. First, we propose a simple lumped modeling method for legged soft robots, by equivalent articulated robots with elastic joints. Another contribution is developing a novel hybrid-quasistatic locomotion analysis which is required to correctly solve statically indeterminate systems with stick-slip contact transitions. Next we show how utilizing our analysis method gives insights regarding the performance of gaits and provides optimal values of gait parameters. Finally, we fabricate and test a fluid-driven soft robot, and obtain good qualitative agreement with the theoretical predictions, proving the applicability of our analysis.

II. QUASISTATIC CRAWLING LOCOMOTION ANALYSIS

We now turn to model the continuous soft mechanism by an articulated three-link robot with torsion springs at its joints, as illustrated in Fig. 3. This section presents the model and analysis of the articulated mechanism's locomotion, while Section III shows the corroboration of the experiments on our soft robot to this analysis.

In our continuous elastic robot shown in Fig. 2, it is observed that each segment bends roughly about its middle. Hence, we choose a three-link configuration with identical uniform distal links, with length l and mass m, and a central uniform link with length $l_0 = \beta l$ and mass $m_0 = \beta m$ (see notations on Fig 3). From the observation above, we have empirically chosen a constant $\beta = 2$. The total length $L = (2 + \beta)l$ and mass $M = (2 + \beta)m$ correspond to the properties of the soft robot, summarized in Table I, from which l and m can be calculated.

In order to account for the elasticity of the continuous structure we introduce equivalent torsion springs at the joints with linear stiffness k, which are at rest when the robot is "flat". To account for the bending actuation of the two beam segments, we apply additional internal input torques $\tau_i(t)$ at the joints (where t is the time). For relative angles between the joints $\boldsymbol{\Phi}(t) = [\varphi_1(t) \ \varphi_2(t)]^{\mathrm{T}}$ and input torques $\boldsymbol{\tau}(t) = [\tau_1(t) \ \tau_2(t)]^{\mathrm{T}}$, the total internal torque at the i-th joint is

$$T_i(t) = \tau_i(t) - k(\varphi_i(t) - \pi). \tag{1}$$

Calibration of the springs' stiffness coefficient and the actuation torques for our soft robot in Fig. 2 is presented in the Supplementary Material [41], and should be performed per specific prototype.

In order to maintain contact with the surface at both ends, the mechanism must satisfy the kinematic relation

$$\sin(\varphi_1 - \theta) - \sin(\varphi_2 + \theta) + \beta \sin \theta = 0, \tag{2}$$

which dictates the absolute orientation angle of the central link $\theta(t)$ as a function of the joint angles $\boldsymbol{\Phi}(t)$ as

$$\tan \theta = \frac{\sin \varphi_1 - \sin \varphi_2}{\cos \varphi_1 + \cos \varphi_2 - \beta}. \tag{3}$$
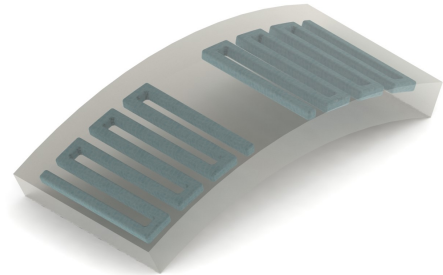

Fig. 2: Schematics of our soft robotic bipedal inchworm-like crawler. The robot consists of an elastic beam containing two segments of embedded fluidic networks, which are separately controlled by time-varying pressure inputs.

The horizontal distance between the contact points is

$$d(t) = l\Big(\beta \cos\theta - \cos(\varphi_1 - \theta) - \cos(\varphi_2 + \theta)\Big). \quad (4)$$

Denoting the center-of-mass horizontal distance from the left contact point (see Fig. 3)

$$x_c(t) \equiv \frac{l}{2(2+\beta)}\Big((2+\beta)\beta\cos\theta - \\ - (3+2\beta)\cos(\varphi_1 - \theta) - \cos(\varphi_2 + \theta)\Big), \quad (5)$$

the static balance of external forces and torques gives the tangential and normal forces, $f_{t,i}$, $f_{n,i}$, at the i-th contact as

$$f_{t,1} = -f_{t,2} \equiv f_t(t) \quad (6a)$$

and

$$f_{n,1}(t) = \left(1 - \frac{x_c}{d}\right)Mg, \quad f_{n,2}(t) = \left(\frac{x_c}{d}\right)Mg, \quad (6b)$$

where g is the gravity acceleration.

It is seen from (6) that the robot is statically indeterminate, and additional considerations are required in order to fully determine the tangential reaction forces f_t. Assuming Coulomb's dry friction model, the tangential forces must maintain

$$|f_{t,i}| \leq \mu f_{n,i} \quad \text{– for a sticking contact} \quad (7a)$$

and

$$|f_{t,i}| = \mu f_{n,i} \quad \text{– for a slipping contact,} \quad (7b)$$

where μ is Coulomb's friction coefficient (for simplicity, we do not distinguish between static and kinetic friction coefficients in this work). Hence, deducing the contact states (stick-stick, stick-slip, slip-stick or slip-slip) resolves the indeterminacy by imposing the tangential forces $f_t(t)$ and hence the configuration $\mathbf{\Phi}(t)$, or vice versa – determining the configuration imposes the forces and dictates the contact states. It is emphasized that such analysis is always required for quasistatic locomotion with two or more frictional contact points.

A. Prescribed angles locomotion

For initial comprehension and simplified analysis of the locomotion, we first consider the case where the trajectories of the two joint angles $\mathbf{\Phi}(t)$ (and hence the angular velocities $\dot{\mathbf{\Phi}}$) are prescribed directly as controlled inputs. In that case the configuration and the kinematics are fully defined, giving

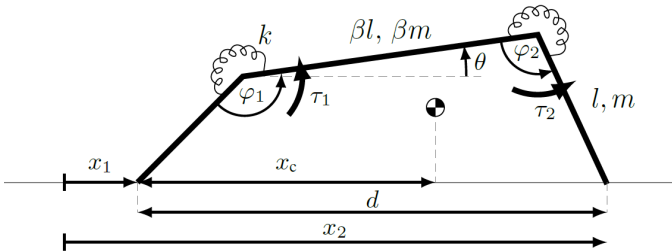Fig. 3: Three-link robot model

the distance between the contact points $d(t)$ (from (4) and (3)) and its time-derivative

$$\dot{d}(t) = l\Big[\sin(\varphi_2 + \theta)(\dot{\varphi}_2 + \dot{\theta}) + \\ + \sin(\varphi_1 - \theta)(\dot{\varphi}_1 - \dot{\theta}) - \beta\sin\theta\,\dot{\theta}\Big]. \quad (8)$$

Since $\dot{d}(t) \not\equiv 0$ for general prescribed angles $\varphi_1(t)$, $\varphi_2(t)$ (except for discrete zero-crossing times), we deduce that at least one of the contacts must slip – which resolves the contact forces as previously mentioned. From (7), assuming all possible combinations of stick and slip contact states for each leg and plugging into (6), it follows that only the contact with the smaller normal force shall slip – which means the foot farther away from the center-of-mass (in the horizontal direction). The slip-slip contacts state (both legs at slippage) is generically impossible in the quasistatic case.

It is deduced that *crawling with passive frictional contacts is generated by shifting the center-of-mass back and forth from one foot towards the other*, which imposes alternating stick-slip transitions at the contacts. We may even denote a slippage criterion variable

$$\Delta(t) \equiv x_c - \frac{d}{2} = \\ = \frac{1+\beta}{2(2+\beta)}l\left[\cos(\varphi_2 + \theta) - \cos(\varphi_1 - \theta)\right], \quad (9)$$

which indicates that when $\Delta = 0$ a switching occurs between right-leg-slippage ($\Delta < 0$) and left-leg-slippage ($\Delta > 0$). From (6) and (7), the tangential forces are obtained as

$$f_t = \mu f_{n,s}\,\text{sign}\,\dot{d}, \quad (10a)$$

where s is the index of the slipping leg

$$s = 1 \quad \text{when} \quad \Delta > 0, \quad (10b)$$
$$s = 2 \quad \text{when} \quad \Delta < 0. \quad (10c)$$

This notion completes the prescribed configuration and kinematics with the contact states.

To illustrate the resulting crawling gaits we study periodic reference inputs $\phi_i(t)$ at the i-th joint of the form

$$\phi_1(t) = \gamma_1 + A_1\sin(\omega t + \psi/2), \quad (11a)$$
$$\phi_2(t) = \gamma_2 + A_2\sin(\omega t - \psi/2), \quad (11b)$$

where γ_i is the nominal angle of the reference input, A_i is the oscillation amplitude and ψ is the phase difference between the inputs. Here, since we assume prescribed joint angles, $\varphi_i(t) \equiv \phi_i(t)$. It is also of note, that as long as the actuation frequency ω is slow enough for the quasistatic assumption to hold, the solution is time-scalable, and ωt in fact only indicates the phase of the cycle. Fig. 4 depicts (in solid curves) the prescribed angles (Fig. 4a) and the resulting positions of the contacts (Fig. 4b) and Fig. 6a depicts the contact forces for one time period $T = 2\pi/\omega$, inputs $\gamma_1 = \gamma_2 = \pi/2$, $A_1 = A_2 = \pi/6$, $\psi = \pi/4$ and the parameters summarized in Table I (which approximate the parameters of the robot in the experimental setup).
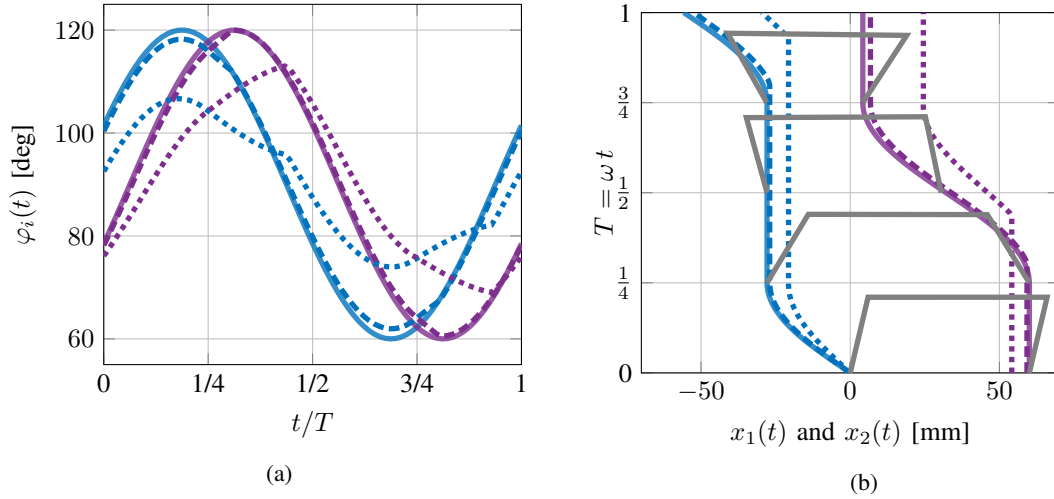
Fig. 4: Simulation solutions for the three-link robot's configuration – Prescribed joint angles (solid curves) vs. prescribed torques with realistic stiffness (dashed curves) and low stiffness (dotted curves). (a) Angles φ_1 (blue) and φ_2 (purple). (b) Position of left x_1 (blue) and right x_2 (purple) contacts and snapshots of the robot (gray)

The simplifying assumption of directly prescribed joint angles, which was presented and analyzed above, is perhaps valid for a robot whose joints can be controlled in closed-loop with a fast response time. However, this is not the case in most soft robotic applications, where usually internal torques are imposed as control inputs. In this case both the contact states and the configuration $\mathbf{\Phi}(t)$ must be determined simultaneously from the prescribed torques $\boldsymbol{\tau}(t)$.

Static balance of torques acting on individual links, considering (6), gives

$$\mathbf{F}(\mathbf{\Phi}, \boldsymbol{\tau}, f_t) \equiv \boldsymbol{\tau} - k \begin{bmatrix} \varphi_1 - \pi \\ \varphi_2 - \pi \end{bmatrix} - l \begin{bmatrix} \sin(\varphi_1 - \theta)) \\ \sin(\varphi_2 + \theta) \end{bmatrix} f_t +$$
$$+ \frac{(1+\beta)l^2 mg}{2\, d(\varphi_1, \varphi_2)} \begin{bmatrix} \cos(\varphi_1 - \theta)(\beta \cos\theta - 2\cos(\varphi_2 + \theta)) \\ \cos(\varphi_2 + \theta)(\beta \cos\theta - 2\cos(\varphi_1 - \theta)) \end{bmatrix} = 0.$$

(12)

This gives two scalar nonlinear transcendental equations $\mathbf{F}(\mathbf{\Phi}, \boldsymbol{\tau}, f_t) = 0$ that relate the prescribed actuation torques $\boldsymbol{\tau}(t)$ to three unknowns – the configuration $\mathbf{\Phi}(t)$ and the tangential force $f_t(t)$.

B. Torque-driven locomotion – Hybrid quasistatics

As explained above, this static indeterminacy is resolved by deducing the contact state, which completes (12) with an additional scalar equation and allows to solve for the configuration $\mathbf{\Phi}$. Then one has to check the solved forces and configuration for consistency of the assumed contacts state or, when inconsistent, deduce a change of the state. The requirements and assumptions of the states is presented next and illustrated in the contacts states' transition graph in Fig 5.

Since $d(t)$ is no longer imposed, $\dot{d}(t)$ can vanish for finite time-intervals, which makes the stick-stick state possible (contact-sticking of both contacts). In such case, an additional kinematic requirement $\dot{d} = 0$ or

$$d(t) = \text{const},$$

(13)

completes (12) and allows for $\mathbf{\Phi}(t)$ and $f_t(t)$ to be (numerically) solved for prescribed actuation torques $\boldsymbol{\tau}(t)$. The assumed stick-stick state is only consistent as long as the calculated tangential force f_t maintains the contact-sticking requirement (7a) at both contacts, i.e.

$$|f_t| \le \mu \min\{f_{n,1}, f_{n,2}\}.$$

(14)

When inequality (14) is crossed, slippage occurs. Following the previous analysis, the contact with the smaller normal force will slip in the direction opposing the friction – i.e. $\text{sign}\,\dot{d} = \text{sign}\,f_t$. For the emerged stick-slip or slip-stick state, the tangential force is now given by (10), which completes (12) and allows to solve for the configuration $\mathbf{\Phi}(t)$. These states are only consistent as long as $\dot{d} \ne 0$, otherwise we return to the stick-stick state governed by (12) and (13). Note that calculating $\dot{d}(t)$ requires differentiating (12) with respect to time to find $\dot{\mathbf{\Phi}}(t)$.

The described solution procedure gives rise to a *hybrid quasistatic* non-smooth system with contact-state transitions (a quasistatic analog of hybrid dynamical systems [42]). Fig 5 depicts the transition graph of the contact states. This analysis allows for continuous (yet non-smooth) contact forces and
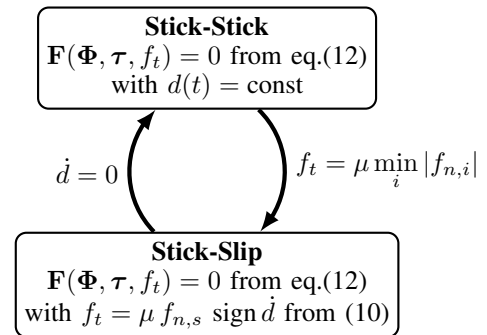

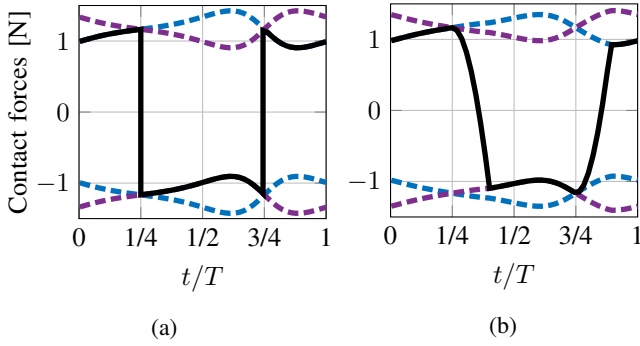Fig. 5: Hybrid-quasistatic system – transition graph of contacts states

Fig. 6: Friction forces limits ($\pm\mu f_{n,1}$ in dashed blue and $\pm\mu f_{n,2}$ in dashed purple) and tangential force f_t (in solid black). (a) Prescribed joint angles simulation. (b) Hybrid-quasistatic simulation

configuration of the robot, without turning to a full dynamical model. It is of note that this nonlinear transcendental system may have multiple solutions. We have implemented a time-stepping numerical algorithm which "tracks" a solution and detects crossing of each contact state's inequalities.

We now turn to illustrate gaits resulting from this analysis. It is convenient to consider torque input of the form

$$\tau_i(t) = k\left(\phi_i(t) - \pi\right). \tag{15}$$

Substituting (15) into (1) gives the total internal torque at each joint as $T_i = -k(\varphi_i - \phi_i)$. This can be interpreted as changing the reference angles of the torsion springs from π to $\phi_i(t)$. The hybrid-quasistatic solution for the configuration $\varphi_i(t)$ is non-smooth and its deviation from the reference trajectories $\phi_i(t)$ depends on the ratio of the tortional stiffness k to the gravitational terms MgL in (12). Fig. 4a shows time plots of the solution for configuration $\Phi(t)$ for the same reference trajectories (11) and parameters of Section II-A. We compare the case of realistic stiffness $k \approx 2.7 MgL$ (dashed curves) and arbitrary low stiffness $k = 0.3 MgL$ (dotted curves). The solid curves depict the solution for the case of prescribed joint angles, which are chosen as identical to the reference trajectories ϕ_i in (15).

We now consider the horizontal position of the two contact points in Fig. 4b. When the angles are prescribed (solid curve), one of the contacts must always be at slippage, while the hybrid solution (under prescribed torques) gives rise to additional intermediate phases of stick-stick contact state, where both contacts are stationary. It is also noticed that the maximal distance between the contacts is smaller than the prescribed angles case, since the hybrid configuration does not reach the maximal amplitude of prescribed reference angles. Moreover, as the ratio k/MgL is lower, the control struggles to impose the reference trajectories, the robot slips less overall, and the distance traveled per step decreases (until reaching full stop below critical stiffness of $k \approx 0.1 MgL$).

Fig. 6a shows how the assumption of prescribed angles results in a discontinuous jump of the contact forces at the instance of switching the slippage direction, which is unrealistic. On the other hand, the hybrid solution in Fig. 6b, involves a finite-time intermediate phase of the tangential forces within the contact-sticking range (14) before switching

slippage direction, thus keeping the forces continuous.

For further intuition on the behaviour of the crawling gaits see Fig. 1 and the supplementary video [43].

C. Parametric study

In order to study the gaits' performance in the parametric-space, we define a sub-class of gaits with *ideal switching* – where one leg only slips during legs' extension ($\dot{d} > 0$) while the other only slips during legs' retraction ($\dot{d} < 0$). This means that $\dot{d}(t)$ and $\Delta(t)$ in (9) cross zero simultaneously, thus maximizing the net distance traveled per step (see Fig. 1)

$$S = \frac{1}{2}\int_0^T \dot{d}(t)\,\mathrm{sign}\Delta(t)\,\mathrm{d}t.$$

In the case where the joint angles are prescribed, it can be analytically proven that ideal-switching gaits are only possible when the angles are symmetrical, i.e. $\gamma_1 = \gamma_2 = \gamma$ and $A_1 = A_2 = A$ in (11), thus reducing the parametric space to (γ, A, ψ). Due to non-linearity of the hybrid case the same conclusion is reached from numeric investigation.

We begin by studying the progression per step S in $\psi - \gamma$ parametric space (for constant amplitude $A = \pi/6$) – depicted in Fig. 7 for the parameters of the experimental setup (Table I). Two nontrivial insights are gained from this contour plot. First, we deduce that the progression is optimal when the nominal angle is $\gamma = \pi/2$. This indicates that an "upright" Π-shaped robot is advantageous for frictional crawling and can be a desired undeformed shapes of such robots, which implies on their structural design.

Second, the progression S decreases monotonically with the phase difference ψ and even vanishes when $\psi \to \pi$. This means that smaller phase difference between the inputs increases the distance traveled per step. An exception is the limit case $\psi = 0$, in which the gait is completely symmetrical and the progression vanishes. Moreover, it is noticed that as the phase difference approaches zero the gait becomes more symmetrical. Practical considerations suggest that such gaits are more sensitive to inaccuracies in the model, particularly in the friction. We perform sensitivity analysis of these results by varying the two friction coefficient at the contacts such that $\mu_1/\mu_2 \in [1-\varepsilon, 1+\varepsilon]$ (where μ_i is the friction coefficient at contact i). Fig. 8 depicts the distance S versus the phase difference ψ (including negative phase difference range) for $\gamma = \pi/2$ and $A = \pi/6$ in solid blue line (note that this is actually a section of the surface plot in Fig. 7). The shaded blue area shows how the distance decreases as the inaccuracy in the friction coefficients rises up to $\varepsilon = 0.1$ (which is close to the actual uncertainty in the friction as measured in Section III). Assuming the friction varies along the gait and among the strides within this uncertainty range, we average the distances in the shaded area by the dashed black curve. This curves shows an optimal phase difference ψ that maximizes the distance S. This also indicates an interesting trade-off between the increasing distance (for ideal conditions) and the sensitivity to friction uncertainties and nonuniformities. Interestingly, these trends also hold for higher friction coefficients, though
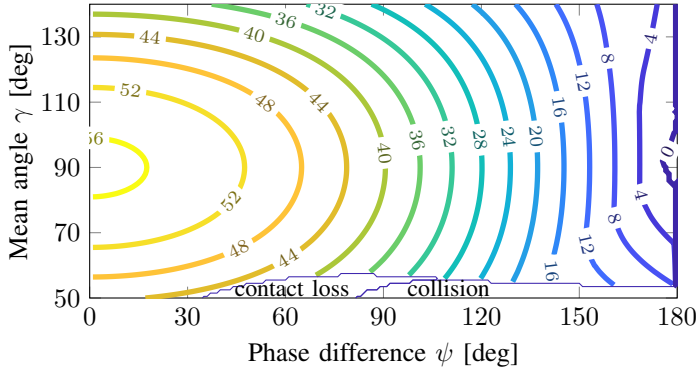
Fig. 7: Net distance per step S[mm] in parametric space $\psi - \gamma$

Fig. 8: Distance per step vs. phase difference – $\mu_1 = \mu_2$ (solid blue curve), $\mu_1/\mu_2 \to 1.1$ (blue area) and average (dashed black)

the progression will stop for certain ranges of parameters (see the Supplementary Material [41] for details).

Another important insight gained from Fig. 8 is the dependence of the direction of the net progression (i.e. the sign of S) on the sign of the phase difference ψ, such that the motion is in the direction of the phase-leading joint. The supplementary video [43] contains experimental demonstration of reversing the crawling direction by reversing the phase difference. This feature enables achieving bi-directional motion of the soft inchworm robot, in contrast to some other works that rely on directional friction by ratchet-like mechanisms [9], [11], [14].

Finally, the distance S rises monotonically with the increase of the amplitude A, as expected – but increasing the amplitude usually involves increased energetic expenditure. To study the gaits' energetic efficiency we define W^+ as the positive work expended by the actuators per cycle, assuming that negative power cannot be stored and regenerated. The positive specific cost of transport [44], given by

$$CoT^+ \equiv \frac{W^+}{Mg\,S},\qquad(16)$$

measures the trade-off between the traveling distance and the energetic cost. Fig. 9 shows the existence of energy-optimal amplitude. Moreover, investigating different stiffnesses k/MgL indicates that a "softer" robot is more energetically efficient, since the springs allow storing more elastic energy from "negative" work, which is otherwise wasted. These insights are of significance in the pursuit of untethered soft-robots. Such robots are required to carry on-board their energy resources, thus energetic consumption poses a challenging problem.

III. EXPERIMENTS

We now turn to investigate by experiments the results achieved from the theoretical parametric study of the lumped model in Section II. As previously introduced, our soft robot consists of a rectangular elastic beam with two embedded slender fluidic networks, which were studied extensively in our previous works [22], [23], [45]. The robot is fabricated by casting Dragon Skin™ silicone rubber over two serpentine cores 3D-printed from PVA, which is water-soluble. Afterwards the cores are dissolved by running water, leaving the required inner cavities. The inlets of both network segments
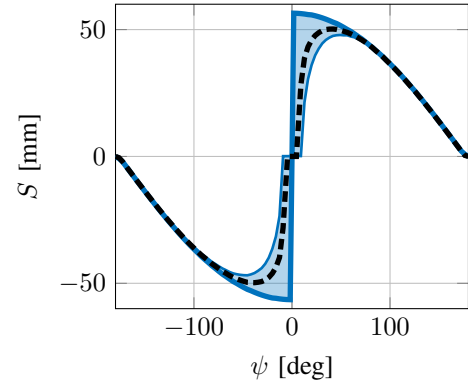
are connected to Elveflow® OB1 MK3 pressure controller in order to impose prescribed pressure functions. For comparison with the analytical results, we investigate periodic pressure inputs of the form (11). Also, since rubber-like materials are known to have complex frictional behaviour which does not fit the simplified dry friction model, smooth masking tape was applied to the contact areas.

Three calibration experiments are performed to fit the torsion springs' linear stiffness coefficient $k = 0.1677$ [Nm/rad] (with $R^2 = 0.989$), a quadratic relation of the pressure to the angle of the form $\varphi_i(t) = a_i\,p(t)^2 + b_i\,p(t)$ (with $R^2 = 0.997$) – where the fitted constants a_i, b_i are summarized in Table I – and the static friction coefficient $\mu = 0.389^{+0.03}_{-0.02}$. The calibration experiments' protocol and results are shown in detail in the Supplementary Material [41].

Periodic pressure inputs of the form (11) are applied. Fig. 10a and Fig. 10b depict the distance traveled per step, normalized by the maximal distance $S/\max\{S\}$, from the experiments (black curve with error bars) and the simulation (blue solid curve) versus the nominal pressure p_0 and the phase difference ψ (respectively).

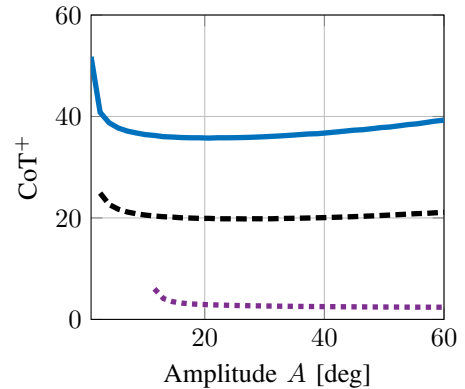The excellent agreement of the normalized distances indi-

Fig. 9: Specific cost of transport vs. torque amplitude – Large stiffness (solid blue curve), realistic stiffness (dashed black curve) and low stiffness (dotted purple curve)

Parameter	Notation	Value	Units
Robot's mass	M	52	gr
Robot's length	L	120	mm
Stiffness coefficient	k	0.1677	Nm/rad
Quadratic pressure coefficients	a_1	0.092	rad/bar^2
	a_2	0.089	rad/bar^2
	b_1	0.127	rad/bar
	b_2	0.144	rad/bar
Friction coefficient	μ	0.389	–

TABLE I: Summary of experimental setup parameters' values

cates that the lumped model and the hybrid-quasistatic solution capture very well the overall crawling mechanism and the influence of the studied gait parameters. Moreover, as the phase difference decreases we observe larger variance in the measured distance and an optimum, as predicted by the sensitivity analysis (Fig. 8).

Yet, it is of note that the non-normalized distance of the robot is about 4 times larger than that of the 3-link model in simulations. This is explained by manufacturing imperfections, which introduce undesired variations in the bending curvature (uneven between the two segments), that cannot be accounted for by the proposed lumped model and shall be addressed in future works. This leads, for example, to non-zero progression at $\psi = 0$, which is supposed to be an ideally symmetric configuration, due to the uncontrolled asymmetry.

IV. CONCLUDING DISCUSSION

This paper has addressed modeling of soft robotic crawling locomotion, proposing an approximation by articulated robots with rigid links and lumped elasticity represented by torsional springs at the joints. Focusing on a quasistatic bipedal crawler with passive frictional contact transitions, which was fabricated by the researchers, a lumped three-link model has been suggested. This system is statically indeterminate, and involves multiple contacts which undergo stick-slip transitions. For quasistatic solution with a continuous configuration of the robot, a novel hybrid analysis has been developed. This modeling method combines kinematic relations and static balances in a non-smooth way, and has been solved by a custom numerical nonlinear time-stepping algorithm.

By simulating the lumped model, comprehension of the crawling mechanism has been achieved, as well as insights on gait-planing and structural design. Practical limitations and energetic considerations have also been discussed. All of those insights (except for the energetic efficiency which was not tested) have shown remarkable qualitative agreement to experiments on our fluid-actuated soft robotic inchworm crawler. This proves the applicability of the proposed modeling and analysis methods to the field of soft legged robots.

On the other hand, the discrepancies between the experiments and the analytical results indicates the high sensitivity and low robustness of the locomotion mechanism of crawling with passive contacts, as have been observed in the experience with our system and by other researchers [27]. A model which better captures the higher order elastic effects but remains lumped enough for analytic insights remains an open challenge which is currently under our investigation.

REFERENCES

[1] S. Kim, C. Laschi, B. Trimmer, Soft robotics: a bioinspired evolution in robotics, Trends in Biotechnology 31 (5) (2013) 287–294.

[2] D. Trivedi, C. D. Rahn, W. M. Kier, I. D. Walker, Soft robotics: Biological inspiration, state of the art, and future research, Applied Bionics and Biomechanics 5 (3) (2008) 99–117.

[3] C. Majidi, Soft robotics: a perspective—current trends and prospects for the future, Soft Robotics 1 (1) (2014) 5–11.

[4] L. I. van Griethuijsen, B. A. Trimmer, Caterpillar crawling over irregular terrain: anticipation and local sensing, J. of Comparative Physiology A 196 (6) (2010) 397–406.

[5] J.-S. Koh, K.-J. Cho, Omegabot: Biomimetic inchworm robot using sma coil actuator and smart composite microstructures (scm), in: Int. Conf. on Robotics and Biomimetics (ROBIO), IEEE, 2009, pp. 1154–1159.

[6] R. F. Shepherd, F. Ilievski, W. Choi, S. A. Morin, A. A. Stokes, A. D. Mazzeo, X. Chen, M. Wang, G. M. Whitesides, Multigait soft robot, Proceedings of the National Academy of Sciences 108 (51) (2011) 20400–20403.

[7] T. Umedachi, V. Vikas, B. A. Trimmer, Highly deformable 3-D printed soft robot generating inching and crawling locomotions with variable friction legs, in: Int. Conf. on Intelligent Robots and Systems (IROS), IEEE/RSJ, 2013, pp. 4590–4595.

[8] S. M. Felton, M. T. Tolley, C. D. Onal, D. Rus, R. J. Wood, Robot self-assembly by folding: A printed inchworm robot, in: Int. Conf. on Robotics and Automation (ICRA), IEEE, 2013, pp. 277–282.

[9] H. Guo, J. Zhang, T. Wang, Y. Li, J. Hong, Y. Li, Design and control of an inchworm-inspired soft robot with Omega-arching locomotion, in: Int. Conf. on Robotics and Automation (ICRA), IEEE, 2017, pp. 4154–4159.

[10] T. Duggan, L. Horowitz, A. Ulug, E. Baker, K. Petersen, Inchworm-inspired locomotion in untethered soft robots, in: Int. Conf. on Soft Robotics (RoboSoft), IEEE, 2019, pp. 200–205.

[11] J. Wang, J. Min, Y. Fei, W. Pang, Study on nonlinear crawling locomotion of modular differential drive soft robot, Nonlinear Dynamics (2019) 1–17.

[12] W. Crooks, S. Rozen-Levy, B. Trimmer, C. Rogers, W. Messner, Passive gripper inspired by manduca sexta and the fin ray® effect, Int. J. of Advanced Robotic Systems 14 (4) (2017) 1729881417721155.

[13] Q. Wu, T. G. D. Jimenez, J. Qu, C. Zhao, X. Liu, Regulating surface traction of a soft robot through electrostatic adhesion control, in: Int. Conf. on Intelligent Robots and Systems (IROS), IEEE/RSJ, 2017, pp. 488–493.

[14] V. Vikas, E. Cohen, R. Grassi, C. Sozer, B. Trimmer, Design and locomotion control of a soft robot using friction manipulation and motor-tendon actuation., IEEE Transaction on Robotics 32 (4) (2016) 949–959.

[15] K. Suzumori, S. Iikura, H. Tanaka, Development of flexible microactuator and its applications to robotic mechanisms, in: Int. Conf. on Robotics and Automation (ICRA), IEEE, 1991, pp. 1622–1627.

[16] K. Suzumori, Elastic materials producing compliant robots, Robotics and Autonomous Systems 18 (1) (1996) 135–140.

[17] A. D. Marchese, D. Rus, Design, kinematics, and control of a soft spatial fluidic elastomer manipulator, The Int. J. of Robotics Research 35 (7) (2016) 840–869.

[18] C. D. Onal, X. Chen, G. M. Whitesides, D. Rus, Soft mobile robots with on-board chemical pressure generation, in: Int. Symposium on Robotics Research, 2011, pp. 1–16.

[19] K. M. de Payrebrune, O. M. O'Reilly, On constitutive relations for a rod-based model of a pneu-net bending actuator, Extreme Mechanics Letters 8 (2016) 38–46.
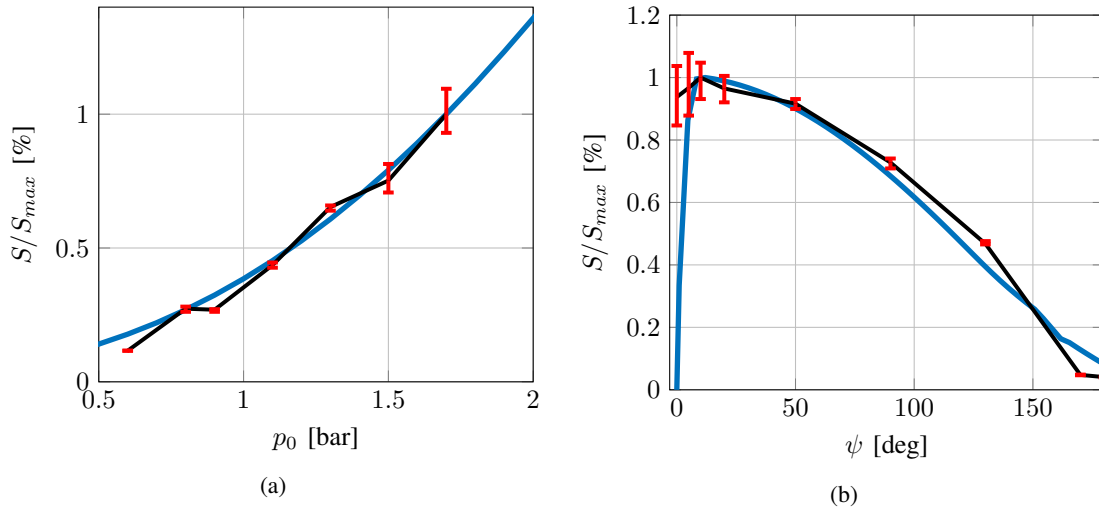
Fig. 10: Experiment results (black) with error-bars (red) and simulation results (blue). (a) Normalized distance traveled per step vs. the nominal pressure. (b) Normalized distance traveled per step vs. the phase difference between inputs.

[20] G. Alici, T. Canty, R. Mutlu, W. Hu, V. Sencadas, Modeling and experimental evaluation of bending behavior of soft pneumatic actuators made of discrete actuation chambers, Soft Robotics 5 (1) (2018) 24–35.

[21] F. Renda, V. Cacucciolo, J. Dias, L. Seneviratne, Discrete cosserat approach for soft robot dynamics: A new piece-wise constant strain model with torsion and shears, in: Int. Conf. on Intelligent Robots and Systems (IROS), IEEE/RSJ, 2016, pp. 5495–5502.

[22] Y. Matia, A. D. Gat, Dynamics of elastic beams with embedded fluid-filled parallel-channel networks, Soft Robotics 2 (1) (2015) 42–47.

[23] B. Gamus, L. Salem, E. Ben-Haim, A. D. Gat, Y. Or, Interaction between inertia, viscosity, and elasticity in soft robotic actuator with fluidic network, IEEE Transactions on Robotics 34 (1) (2018) 81–90.

[24] A. D. Marchese, C. D. Onal, D. Rus, Autonomous soft robotic fish capable of escape maneuvers using fluidic elastomer actuators, Soft Robotics 1 (1) (2014) 75–87.

[25] D. Drotman, S. Jadhav, M. Karimi, M. T. Tolley, et al., 3d printed soft actuators for a legged robot capable of navigating unstructured terrain, in: Int. Conf. on Robotics and Automation (ICRA), IEEE, 2017, pp. 5532–5538.

[26] R. K. Katzschmann, A. D. Marchese, D. Rus, Hydraulic autonomous soft robotic fish for 3d swimming, in: Experimental Robotics, Springer, 2016, pp. 405–420.

[27] C. Majidi, R. F. Shepherd, R. K. Kramer, G. M. Whitesides, R. J. Wood, Influence of surface traction on soft robot undulation, The Int. J. of Robotics Research 32 (13) (2013) 1577–1584.

[28] D. W. Schuldt, J. Rife, B. Trimmer, Template for robust soft-body crawling with reflex-triggered gripping, Bioinspiration & biomimetics 10 (1) (2015) 016018.

[29] F. Saunders, B. A. Trimmer, J. Rife, Modeling locomotion of a soft-bodied arthropod using inverse dynamics, Bioinspiration & biomimetics 6 (1) (2010) 016001.

[30] F. Saunders, E. Golden, R. D. White, J. Rife, Experimental verification of soft-robot gaits evolved using a lumped dynamic model, Robotica 29 (6) (2011) 823–830.

[31] X. Zhou, C. Majidi, O. M. O'Reilly, Energy efficiency in friction-based locomotion mechanisms for soft and hard robots: Slower can be faster, Nonlinear Dynamics 78 (4) (2014) 2811–2821.

[32] X. Zhou, C. Majidi, et al., Flexing into motion: A locomotion mechanism for soft robots, Int. J. of Non-Linear Mechanics 74 (2015) 7–17.

[33] N. N. Goldberg, X. Huang, C. Majidi, A. Novelia, O. M. O'Reilly, D. A. Paley, W. L. Scott, On planar discrete elastic rod models for the locomotion of soft robots, Soft robotics.

[34] L. L. Howell, Compliant mechanisms, John Wiley & Sons, 2001.

[35] A. DeMario, J. Zhao, Development and analysis of a three-dimensional printed miniature walking robot with soft joints and links, J. of Mechanisms and Robotics 10 (4) (2018) 041005.

[36] J. Y. Jun, J. E. Clark, A reduced-order dynamical model for running with curved legs, in: Int. Conf. on Robotics and Automation (ICRA), IEEE, 2012, pp. 2351–2357.

[37] L. Paez, G. Agarwal, J. Paik, Design and analysis of a soft pneumatic actuator with origami shell reinforcement, Soft Robotics 3 (3) (2016) 109–119.

[38] T. McGeer, et al., Passive dynamic walking, The Int. J. of Robotics Research 9 (2) (1990) 62–82.

[39] J. R. Usherwood, S. B. Williams, A. M. Wilson, Mechanics of dog walking compared with a passive, stiff-limbed, 4-bar linkage model, and their collisional implications, J. of Experimental Biology 210 (3) (2007) 533–540.

[40] A. D. Marchese, R. K. Katzschmann, D. Rus, A recipe for soft fluidic elastomer robots, Soft Robotics 2 (1) (2015) 7–25.

[41] Supplemental material at https://arxiv.org/abs/1911.05227.

[42] R. Goebel, R. G. Sanfelice, A. R. Teel, Hybrid dynamical systems, Control Systems Magazine 29 (2) (2009) 28–93.

[43] Supplemental video at https://www.youtube.com/watch?v=ohybly7uaao.

[44] S. Collins, A. Ruina, R. Tedrake, M. Wisse, Efficient bipedal robots based on passive-dynamic walkers, Science 307 (5712) (2005) 1082–1085.

[45] Y. Matia, T. Elimelech, A. D. Gat, Leveraging internal viscous flow to extend the capabilities of beam-shaped soft robotic actuators, Soft Robotics 4 (2) (2017) 126–134.

This supplementary material describes in more details the calibration experiments' protocol and results, omitted from the main paper for brevity, and illustrates the presented result regarding the influence of higher friction on the observed trends in phase difference ψ.

Calibration experiments

Three calibration experiments are performed, as follows: in order to find the stiffness coefficient k we clamp the robot at the center, apply a vertical force f at the edge (at $x = L/2 \equiv w$) via a force gauge and measure the vertical deflection of the edge z utilizing millimetric paper. We then calculate the angle of the edge from the deflection $\varphi = \sin^{-1} z/w$ and the torque resulting from the force $M = f \, w \cos \varphi$. We fit a torsion spring with linear stiffness coefficient $k = 0.1677$ [Nm/rad] with good agreement $R^2 = 0.989$ (see Fig. 11).

Next, for the same clamped configuration, we introduce gauged pressure into each channel segment by the controller, and again measure the vertical deflection z of the edge. We relate the input pressure to the angle φ_i of the edge of each segment i separately (while the other segment is clamped). The angle is then related to the torque applied by the input pressure via the previously measured stiffness k. A linear regression of the form $\varphi_i(t) = \alpha_i \, p(t)$ fits with fair agreement $R^2 = 0.942$. Yet, performing the experiments for a significant range of pressures p_0 requires achieving large deformations (about 50% of the actuator's length). At this range, a quadratic relation of the pressure to the angle of the form $\varphi_i(t) = a_i \, p(t)^2 + b_i \, p(t)$ fits with better agreement $R^2 = 0.997$ (see Fig. 12).

Finally, the static friction coefficient μ is estimated by varying the slope angle of an inclined plane with the robot standing on top, and recording the angle when the robot starts to slip. The static friction coefficient is given by the tangent of the measured angle. By repeating this experiment several times the coefficient was measured as $\mu = 0.389^{+0.03}_{-0.02}$.
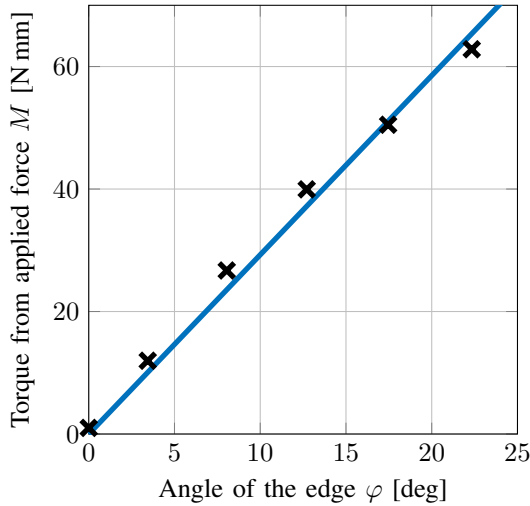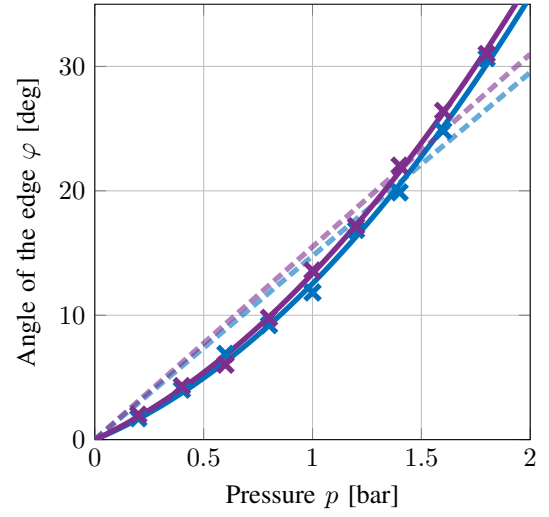

Fig. 12: Pressure calibration experiment – Left segment in blue and right segment in purple. Measured data in 'x', fitted linear curve in dotted light curve and quadratic curve in solid curve

Influence of higher friction

We have also numerically investigated the influence of higher friction coefficient on the trends we discussed in the paper. Interestingly, our observations hold, and the progression S still decreases monotonically with the phase difference ψ (see Fig. 13). Yet, as the friction rises, the robot's progression stops for a growing range of ψ. This is due to the fact that this analysis (and the actual robot) are torque-driven, and as the friction rises the system struggles to follow the trajectory prescribed by the torques. The actual angles' amplitude becomes smaller, and the movement and progression per step nulls.

Fig. 11: Stiffness calibration experiment – Measured data in 'x' and fitted linear curve in solid blue
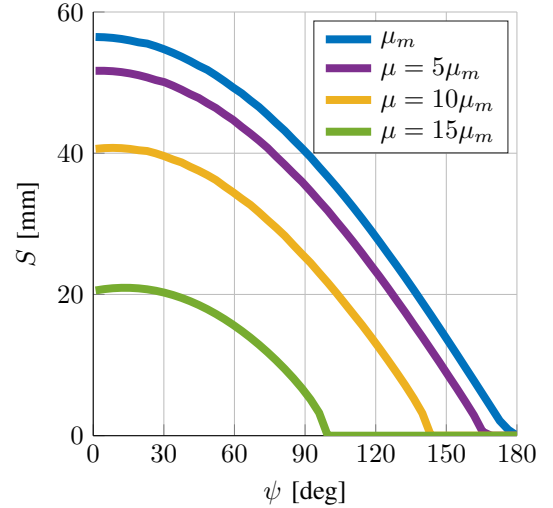

Fig. 13: Distance per step vs. phase difference – Measured friction $\mu_m = 0.389$ (solid blue curve) and multiplications of it